Emre Dikmen
e-mail: edikmen@gmail.com

Peter J. M. van der Hoogt
e-mail: P.J.M.vanderHoogt@ctw.utwente.nl

André de Boer
e-mail: a.deboer@utwente.nl

Faculty of Engineering Technology,
Section of Applied Mechanics,
University of Twente, P.O. Box 217,
7500 AE Enschede, The Netherlands

Ronald G. K. M. Aarts
e-mail: R.G.K.M.Aarts@ctw.utwente.nl

Ben Jonker
e-mail: J.B.Jonker@ctw.utwente.nl

Faculty of Engineering Technology,
Section of Mechanical Automation,
University of Twente, P.O. Box 217,
7500 AE Enschede, The Netherlands

Design of an Experimental Setup for Testing Multiphysical Effects on High Speed Mini Rotors

*Recently, there have been numerous research projects on the development of minirotating machines. These machines mostly operate at speeds above the first critical speed and have special levitation systems. Besides, the multiphysical effects become significant in small scale. Therefore, advanced modeling approaches should be developed and innovative experimental rigs with the foregoing requirements should be constructed in order to test the developed techniques. In the current study, the design of an experimental setup for testing the multiphysical effects has been outlined. First, the previously developed multiphysical models (Dikmen, E., van der Hoogt, P., de Boer, A., and Aarts, R., 2010, "Influence of Multiphysical Effects on the Dynamics of High Speed Minirotors—Part I: Theory," J. Vibr. Acoust., **132**, p. 031010; Dikmen, E., van der Hoogt, P., de Boer, A., and Aarts, R., 2010, "Influence of Multiphysical Effects on the Dynamics of High Speed Minirotors—Part II: Results," J. Vibr. Acoust., **132**, p. 031011) for the analysis of small scale rotors are described briefly for background information. Second, an analysis of the effect of the rotor parameters (diameter, length, rotation speed, etc.) on the dynamics of the rotor under multiphysical effects is presented. Afterward the design process which includes the design decisions based on these results, the availability, simplicity, and applicability of each component is presented in detail. Finally, the experimental results have been presented and the efficiency of the design has been evaluated. In summary, the design requirements for an experimental setup for testing multiphysical effects on minirotors have been analyzed. The design procedure and evaluation of the design have been presented.* [DOI: 10.1115/1.4004003]

1 Introduction

The trend in the engineering field for rotating machinery is to design smaller and faster machines. There has been extensive research for the development of these machinery worldwide: microturbines [1–5], flywheels for microsatellites [6,7], and ultra-high speed drives [8–10]. Although these machinery are called micro, they are in milimeter scale. The diameters change from 5 to 10 mm [4,5,10]. Multiphysical effects such as interaction with the surrounding air and thermal effects become significant on the dynamics of these applications with the changing scale [3,11]. In Refs. [12, 13], we modeled the physical effects resulting from the air in the closed confinement between a rotor and its casing and investigated their coupled influence on the dynamics of high speed minirotors.

For the experimental validation of these models, a dedicated test-rig has to be designed. In literature on the design of minirotating machinery [3,4,8,9], the focus is mostly on the efficiency of a specific application. Only a few papers address testing the dynamic behavior of high speed minirotating machinery under the influence of other physical phenomena [14–16]. There is no information about general experimental setups to test the multiphysical effects on the rotordynamics in small scale. This paper identifies the design requirements and design considerations toward an experimental setup for the analysis of the dynamic behavior of minirotors.

The main contribution is the determination of the design requirements and considerations to built a novel experimental setup for testing the multiphysical effects on small scale rotordynamics (Secs. 3–5).

Contributed by the Design Innovation and Devices Committee of ASME for publication in the JOURNAL OF MECHANICAL DESIGN. Manuscript received May 21, 2010; final manuscript received March 31, 2011; published online xx xx, xxxx. Assoc. Editor: Alexander Slocum.

2 Multiphysical Rotordynamics Model

As stated above, the aim of designing the setup is to test the previously developed multiphysical rotordynamics model. This model includes a structural model for the rotor, the flow induced force for systems with the medium sized gaps and a thermal model which predicts the heat generation and temperature of the air in the gap between the rotor and the casing. The developed multiphysical modeling approach will be explained briefly below. More detailed explanation has been provided in the previous papers [12,13].

2.1 Structural Model. The structural model is based on the finite element method (FEM) using the Timoshenko beam formulation [17,18]. The beam element has two nodes, one at each end and has six degrees of freedom (three translational and three rotational) per node with uncoupled axial, torsional, and flexural behaviors.

In our study, axial and torsional vibrations are ignored; so only flexural behavior of the rotor is taken into account, reducing the number of degrees of freedom (DOF) to four at each node (Fig. 1). The use of complex notation makes calculations more convenient, so the vector of nodal displacements of the element is given by:

$$\mathbf{q} = [u_{x_1} + iu_{y_1}, \phi_{y_1} - i\phi_{x_1}, u_{x_2} + iu_{y_2}, \phi_{y_2} - i\phi_{x_2}]^T$$

With the use of shape functions consistent stiffness, mass and gyroscopic matrices for a beam element have been derived by Genta [19]. These matrices are assembled leading to the governing equation of motion for the structure. A MATLAB code is developed to calculate and assemble the element matrices. Next, the eigenvalues are calculated to determine the natural frequencies and the onset of instability.

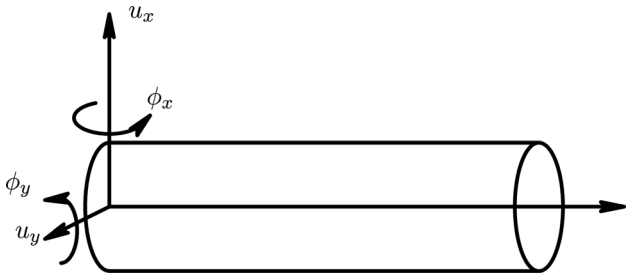

Fig. 1 Beam element

2.2 Fluid Model. The gap size between the rotor and the casing in microrotating machinery is mostly moderate in comparison to the smaller gaps in bearings and seals (see Fig. 2). The bearings and seals are widely studied, and for these systems, the inertia effects can be neglected. On the other hand, in minirotating machinery, there are large clearances and high rotation speeds making inertia effects significant [1]. Antunes et al. [20] obtained linearized flow induced forces per unit length for a fluid annulus with medium gap size using perturbation methods with an empirical shear stress, assuming two dimensional flow and accounting for the inertia terms. These forces are given in terms of added mass, stiffness, and damping matrices that can easily be implemented into the structural model.

2.3 Thermal Model. Due to the high rotation speeds, the flow causes large amounts of power loss. This power loss is caused by the air friction and it can be calculated using semi-empirical friction coefficients. The relations between friction coefficient c_f, shear stress τ, and heat dissipation P are given as [21]:

$$c_f = \frac{\tau}{\frac{1}{2}\rho\Omega^2 r^2} \tag{1}$$

$$P = c_f \pi \rho \Omega^3 r^4 l \tag{2}$$

where l is the length of the rotor, Ω is the rotation speed, and r is the rotor radius. Thermal resistance network method has been used to model the rotor, the air gap, and the casing. These networks consist of nodes describing the mean temperature of each component and of resistances between the nodes. The thermal networks representing the rotor, the casing and the node representing the air in between are assembled. The heat generation is applied to the node representing the air gap, and the air gap temperature is calculated at each rotation speed.

2.4 Combining Multiphysical Models. The developed thermal model is used to calculate the heat generation and air temperature in the gap at each rotation speed. This temperature is used to update the air properties (density and viscosity) and, hence, the friction coefficient, which is required for the calculation of the flow induced forces. Finally, the flow induced forces are implemented into the structural model. In this way, a coupled analysis of three physical domains is performed. The procedure for the coupling of these domains is given in Fig. 3.

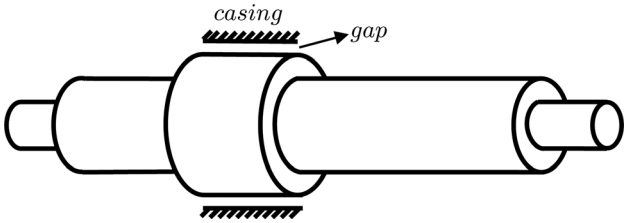

Fig. 2 Thermal networks

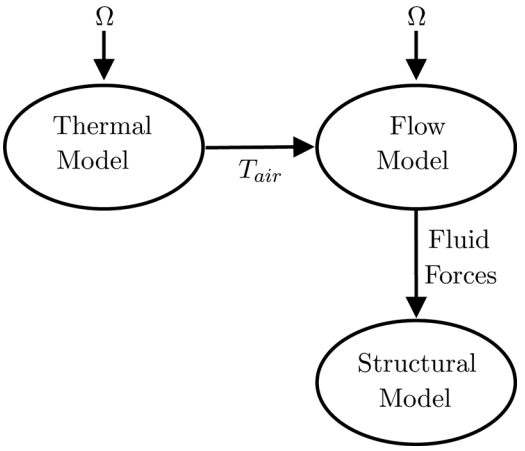

Fig. 3 Coupling procedure

3 Analysis of the Rotor Parameters

The multiphysical effects on the dynamics of the rotor are investigated for different geometries, various gap sizes, and different support stiffnesses to determine the design parameters. To observe the effect of each parameter, the other parameters should be kept constant. Therefore, an initial geometry, support stiffness, speed, and clearance are used in the simulations as shown in Table 1 and Fig. 4. Microrotating machinery have mostly small shaft diameters (5–10 mm) and high speeds (100,000–300,000 rpm). However, similar flow conditions occur at low speeds with larger diameter. The geometrical parameters are determined in order to investigate whether the multiphysical effects are visible at lower speeds. The damping ratio is equal to 1%, which is a reasonable value for steel components.

3.1 Rotation Speed. The simulations with and without casing are compared to observe the dynamic behavior due to flow induced effects. For simulations without stator, so without an air gap, the fluid and thermal models are not used. The simulations are performed in a range of rotation speeds. The Campbell diagrams with and without fluid are given in Fig. 5. This diagram illustrates the change of the natural frequencies with rotation speed, Ω, and reveals the critical speeds. It can be observed that only the first natural frequency changes significantly. The flow induced effects become more important with increasing Ω A summary of these results is listed in Table 2.

3.2 Clearance. The clearance between the casing and the rotor affects the flow induced forces; therefore, the size of the gap is significant for the rotordynamic behavior. That is why the simulations have been performed for three different clearances. The onset of instability and the first natural frequencies are listed in Table 3. The onset of instability is determined by using the decay rate plots. As the decay rates become negative, the vibrations are

Table 1 System parameters and friction torque

Rotation speed	50,000	rpm
Clearance	0.5	mm
Disk diameter	40	mm
Disk length	30	mm
Diameter-near disk	15	mm
Diameter-shaft	6	mm
Near disk length	10	mm
Total length	150	mm
Support stiffness	10^5	N/m
Damping	1	%

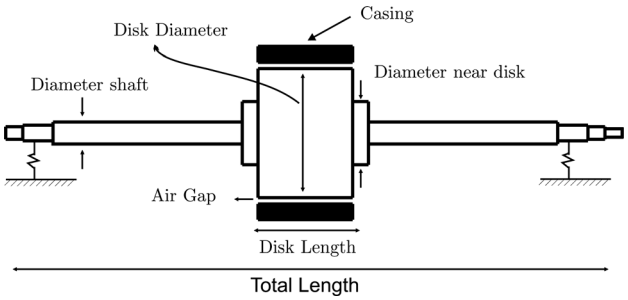

Fig. 4 Rotor parameters

not damped out. Instead self excitation which results in instability of the system occurs.

As the clearance decreases, the flow-induced effects become more important. The natural frequencies do not change significantly. However, the onset of instability changes drastically.

3.3 Disk Diameter. The disk diameter, D_d, is another important design parameter. It has a significant contribution on the disk surface velocity and thus on the flow induced forces and the flow regime. The simulation results for different disk diameters are given in Table 4. As the diameter increases, the surface velocity increases linearly and the flow induced effects become more dominant. The decay rate graphs are given in Fig. 6 for $D_d = 30$ and 60 mm, respectively. As the decay rate becomes negative, self excited vibrations occur and the system becomes unstable.

3.4 Disk Length. The disk length, l, is also an important design criterium. It alters the mass of the rotor and consequently the natural frequencies. Besides it is confined in the casing and it determines the surface area of the rotor under the influence of fluid. Simulations are performed for different lengths and the results are shown in Table 5.

3.5 Support Stiffness. The support stiffness determines the critical speeds and the mode shapes. In Table 6, the first three critical speeds till 200,000 rpm are given for different support stiffnesses. In Fig. 7, the mode shapes corresponding to the first natural frequency are given for different support stiffnesses. The support stiffness changes the mode shapes and the critical speeds radically. For support stiffnesses of 10^6 and 10^7 N/m, the rigid body modes are not observed and the second and third critical speed changes significantly.

Table 2 First natural frequency at different rotation speeds

Rotation speed	rpm	1000	30,000	50,000	60,000	80,000	100,000
Without air	rad/s	692.1	692.1	692.1	692.1	692.1	692.1
With air	rad/s	692.0	690.0	682.1	676.0	659.2	636.3
Difference	%	0.01	0.30	1.44	2.32	4.75	8.06

4 Temperature Increase and Friction Torque

The air in the gap results in friction losses as explained in Secs 1–3. The amount of power loss and torque should be known in advance in order to select the motor which can reach the desired operation speeds. The air friction loss due to the shaft itself is much less compared to the disk, since the shaft diameter is much smaller. For different disk diameters, disk lengths, spin speeds, and air gaps, the air gap temperature, power loss, and friction torque are calculated. For a standard, geometry (Table 1) these results are listed in Table 7. The maximum rotation speed and the disk diameter have the largest effect on the friction torque.

5 Design Process

5.1 Requirements. The aim of this study is to design an ideal experimental setup in which the multiphysical effects on the dynamics of the microrotating machinery can be investigated. The onset of instability resulting from the surrounding fluid should be observed in the operation range. The design criteria have been determined by considering the analysis in Sec. 4. The requirements for each parameter are listed below:

(1) Rotation speed (Ω): Must be high enough to observe instability. Besides the maximum rotation speed should be in the operation range of the motor and flexible coupling.
(2) Gap size (H): Must be determined such that the gap ratio (H/r) is different from the bearings and seals. Flow induced instability could be measurable in the operation range.
(3) Disk diameter (D_d): Must be determined to result in similar flow conditions as the microrotating applications in the literature. Besides the disk diameter should be selected such that the instability can be observed in the operation range.
(4) Disk length (l): The disk length must be selected such that the air friction torque is low but still the multiphysical effects are observable.
(5) Shaft diameter (D_s): Must be low such that the flexural mode natural frequency can be measured.

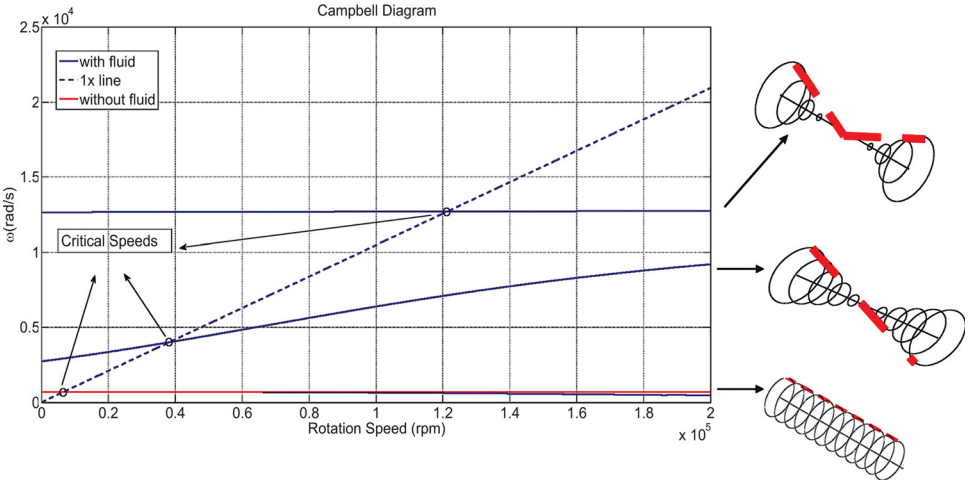

Fig. 5 Campbell diagram

Table 3 Natural frequencies at 50,000 rpm and onset of instability

Clearance	[mm]	0.25	0.50	0.75
Gap ratio (H/r)	—	1/80	1/40	3/80
First natural frequency	rad/s	671.8	682.1	685.0
Difference	%	2.93	1.45	1.02
Onset of instability	rpm	28,800	62,000	102,100

Table 4 Natural frequencies at 50,000 rpm and onset of instability for different disk diameter

Diameter	[mm]	30	40	50	60
Gap ratio (H/r)	—	1/30	1/40	1/50	1/60
First natural frequency	rad/s	873.3	682.1	549.4	450.7
Difference	%	0.55	1.45	3.21	6.05
Onset of instability	rpm	106,600	62,000	40,300	28,700

(6) Rotor length (L): Must be determined such that the air friction torque is negligible but still the modeled phenomenon is observable.
(7) Support stiffness (k): Most of the applications in the literature involve air bearings or magnetic bearings with low support stiffness. The support structure must be designed to have similar support properties to mimic these applications and enable the measurement of instability in the operation range.

Studying the temperature increase in the air gap is not a design criterion because from the previous analysis (Table 7), it can be seen that the increase in temperature can not be easily observed with a feasible design. Besides accurate measurements of air temperature could be quite difficult. The high rotation speeds, the complex flow and the small gap prevent locating the sensor for temperature measurement. Therefore, the thermal model has been verified by comparing it with a CFD model [22].

5.2 Component Design

5.2.1 Motor. There are different ways to drive the rotor. A pelton impulse turbine has been used in the preliminary design of microturbines. High rotation speeds (160,000 rpm) and driving torques can be achieved [6]. However, the design and manufacturing of blades are complex and require a long design process. Another option is to use a permanent magnet motor. This motor consists of magnets attached to the rotor and a stator made of windings reaching high speeds of 170,000 rpm. Only the stator and permanent magnets are commercially available in the market, from which the complete motor should be built by the client. Furthermore, this choice results in long delivery time. The third option is to use a brushless motor. This is a complete motor with an output shaft and makes use of windings and magnets. A disadvantage of this motor is the lower maximum speed, which is limited by the bearings in the motor and a coupling is needed to connect the output shaft to the rotor.

Table 5 Natural frequencies at 50,000 rpm and onset of instability for different disc lengths

Disk length	mm	10	20	30	40
First natural frequency	rad/s	1064.0	815.2	682.1	595.3
Onset of instability	rpm	—	93,700	62,000	48,600

Table 6 The critical speeds for different support stiffness

Stiffness	[N/m]	10^5	10^6	10^7
First critical speed	rpm	6400	12,700	14,800
Second critical speed	rpm	38,300	104,900	152,400
Third critical speed	rpm	121,800	196,000	Above 200,000

This option has been selected since it is easily accessible in the market and simple to be implemented into the experimental setup. A speed of 50,000 rpm could be enough to observe the multiphysical effects as the disk diameter is increased as seen from Table 4. This enables to have similar flow conditions as exists in smaller micromachinery with higher rotation speeds. Besides in Table 2, it is observed that the change in natural frequency is not significant even at a speed of 100,000 rpm and the unstable operation can happen before reaching this speed. Therefore, it is decided to use a motor with a maximum operation speed of 50,000 rpm and adjusting the disk diameter, D_d, the clearance and the other parameters analyzed in Sec. 3 so that the onset of instability can be determined.

A Maxon EC 22 motor has been used for the current application. The EC 22 motor has three hall sensors to locate the orientation of the output shaft. The hall sensors provide information about the rotation speed. This information is sent to an amplifier. This unit also controls the speed, acceleration, and direction of the motor. The motor is clamped on an aluminum block.

5.2.2 Rotor. The dimensions of the rotor have been determined so that the critical speeds and the unstable operation can be

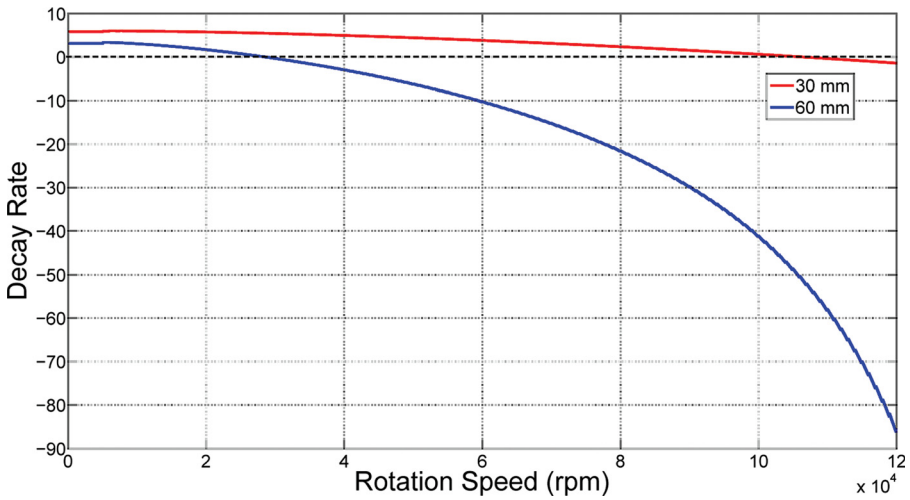

Fig. 6 Decay rates for disk diameter of 60 and 30 mm

Table 7 System parameters and friction torque

Disk diameter	mm	10	20	30	40	50	60
Temperature	K	293.2	293.8	294.8	295.7	297.1	299.7
Torque	mNm	0.02	0.16	0.56	1.42	2.91	5.21
Disk length	mm	10	20	30	40	50	60
Temperature	K	295.7	296.0	295.7	295.7	295.7	295.7
Torque	mNm	0.47	0.95	1.42	1.90	2.37	2.85
Rotation Speed	Krpm	20	40	50	60	80	100
Temperature	K	293.4	294.7	295.7	296.9	300.2	304.6
Torque	mNm	0.36	1.02	1.42	1.88	2.88	4.03
Clearance	mm	0.20	0.25	0.30	0.40	0.50	0.6
Temperature	K	295.7	295.7	295.7	295.7	295.7	295.7
Torque	mNm	1.71	1.63	1.58	1.49	1.42	1.37

observed within the operation range. The final geometry is shown in Fig. 8. A disk diameter of 50 mm results in significant flow induced effects as can be seen in Table 4. A larger diameter would be even more significant, but it would increase the amount of torque required for the motor. The total length of the rotor is 195 mm with a nominal shaft diameter of 7 mm. The length of the disk has been determined to be 30 mm. As in that case the multiphysical effects are significant. Making the disk length longer increases the multiphysical effects only slightly (see Table 5), this however results in more friction torque. Due to the high difference in diameter between the shaft and the disk, the diameter of the rotor is locally increased to 20 mm near the disk. This results in lower stresses in the rotor. The diameter of the shaft at the bearing locations is 5 mm in order to mount the bearings. An M4 nut locks the other side of the inner ring. The right side of the rotor has an additional part with a diameter of 3 mm to mount the coupling. The tolerances on the bearing seats are based on the information provided by the bearing company. The rotor has been manufactured with strict tolerances and from one piece in order to reduce eccentricity and unbalance. High performance steel DIN 1.2510 hardened at 50 HR is used in order to achieve better surface quality and to increase the yield strength.

5.2.3 Bearing. Due to high rotation speeds and friction losses, contactless (air or magnetic) bearings [23,24] or special ball bearings are used for the high speed minirotating machinery [10]. Aerostatic, aerodynamic, and air foil bearings work on external pressure or rotor rotation. The operation is contactless and the amount of friction loss is less than the traditional levitation

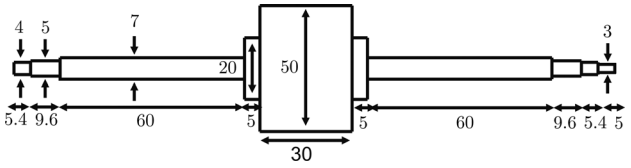

Fig. 8 The dimensions of the rotor

systems. However, they are not commercially available and they require detailed, complex analysis to design and manufacture. Magnetic bearings use magnetic forces to levitate the rotor. They have the same advantages as the gas bearings, but they require sensors and control units. Besides they are not commercially available for standard solutions. High speed ball bearings are available commercially at small size, robust and do not require extra equipment. More friction than contactless bearings and limited operation temperatures are the main disadvantages. However due to robustness, availability in the market, simplicity of mounting and operating at high speed, angular contact ball bearings are selected for this experimental setup. Angular contact bearings are also capable of supporting the axial loads. In this study, the GMN S625 C TA bearings are used, which enable safe operation above 100,000 rpm. This bearing consists of balls made from chrome steel, an inner ring with two shoulders, an outer ring with one shoulder and a cage made from textile-reinforced phenolic resin between these rings.

5.2.4 Coupling. A coupling is needed to connect the motor to the rotor. This coupling should be flexible; otherwise, the vibrations will be transmitted to the motor and the motor could be damaged. The torque delivered by the motor has to be transferred to the rotor by using the coupling. Therefore, the coupling is stiff in the rotating axis and flexible in the radial axis. The coupling KTR Rotex GS 5 is used to connect the motor to the rotor. The coupling consists of three parts: two metal hubs and a flexible plastic spider in between. The coupling is illustrated in Fig. 9. One hub is connected to the motor and the other to the rotor. This can be done by gluing or clamping with a bolt. Gluing is a better solution, since the bolt introduces an extra unbalance. The choice of the spider is also important, because a more flexible spider can absorb more axial, angular, and radial misalignment but can handle less torque. The most flexible spider can handle 300 mNm, which is much higher than the driving torque at maximum speed (15 mNm).

5.2.5 Flexible Support. As explained before most of the high speed microrotating machinery have contactless bearings which

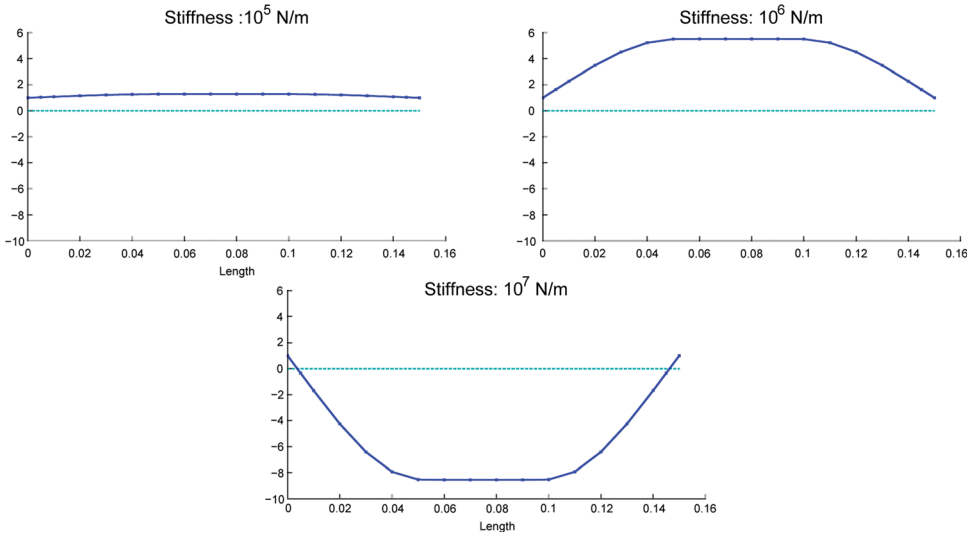

Fig. 7 Mode shape for the first natural frequency at different stiffness

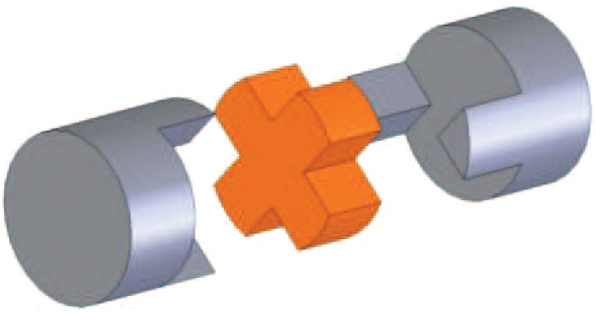

Fig. 9 Coupling

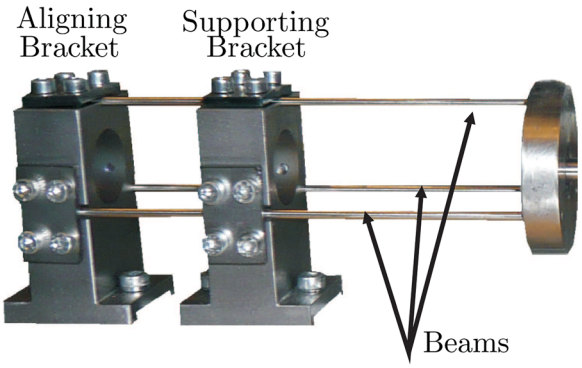

Fig. 10 Flexible supports

have lower support stiffness compared to conventional supports. Besides from the previous analysis, it has been observed that the support stiffness should be in the order of 10^5 N/m in order to observe the multiphysical effects. The radial stiffness of the ball bearings are around $10^7 - 10^8$ N/m. Therefore, an extra support system is required to decrease the support stiffness of the rotor. A solution to decrease the support stiffness of the rotor is to build a flexible support between the bearing and the fixed frame. The support structure must be radially isotropic and axial movement must be prevented. This flexible support can be made of beams or leaf springs. The stiffness of this bearing support can be changed by elongating these beams or leaf springs. Another solution is to use flexible rings between the bearing and the bearing housing [25]. However, these rings are made of plastic or rubber and are not available on the market. Besides, it is difficult to manufacture isotropic rings. Furthermore for each new experiment, these rings should be replaced by rings with a different stiffness and the whole setup should be aligned again in order to perform experiments with different support stiffnesses. A different solution to decrease the stiffness is hanging the bearings on springs. However, the springs can easily bend and the bearing housing can tilt resulting in alignment problems and extra friction.

Table 8 Support stiffness for different beam lengths

Beam length (mm)	72 mm	80 mm	90 mm
Stiffness (N/m)	7.03×10^4	5.16×10^4	3.36×10^4

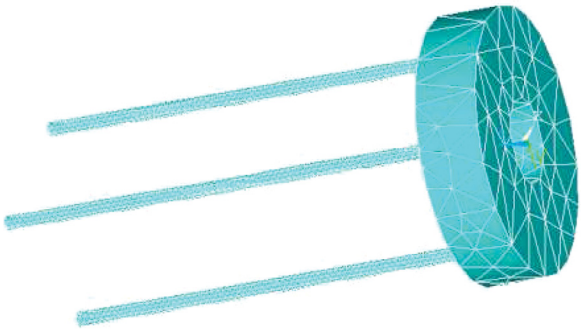

Fig. 11 ANSYS model of the support

Finally, a robust support which provides isotropic radial stiffness has been designed. The flexible support includes three support beams, a support disc in which the bearings are located and two brackets as shown in Fig. 10. The supporting bracket can be moved to another position thus changing the beam length. In this way, the support stiffness that changes the rotordynamic behavior can be adjusted. The aligning bracket avoids alignment problems during this process. An Ansys model has been developed to determine the stiffness and the support beam lengths are determined accordingly (see Fig. 11). The stiffness results obtained from finite element analysis are provided in Table 8.

6 Evaluation of the Design

6.1 Comparison With the Other Applications. The final design of the setup is shown in Fig. 12 [13]. The maximum operation speed is 50,000 rpm. The reduced natural frequency and reduced decay rate are considered for this setup and a microgenerator which has a length of 55 mm, diameter of 6 mm, and maximum operation speed of 500,000 rpm [8]. The simulations have been performed for different support stiffness of the microgenerator. The same damping ratio as the setup is used for the microgenerator simulations. The natural frequency is the real part (ω) and the decay rate (σ) is the imaginary part of the complex frequency (eigenvalue) $\lambda = \omega + i\sigma$, where $e^{i\lambda t}$ is the solution of the homogeneous equation of motion of the rotor given below.

$$\mathbf{M}\ddot{\mathbf{q}} + (\mathbf{C} - i\Omega\mathbf{G})\dot{\mathbf{q}} + (\mathbf{K} - i\Omega\mathbf{C}_r)\dot{\mathbf{q}} = 0 \tag{3}$$

When the decay rate becomes negative, the system becomes unstable. The reduced natural frequency ($\bar{\omega} = \omega/\omega_1$) and the reduced decay rate ($\bar{\sigma} = \sigma/\sigma_1$) are plotted in Figs. 13 and 14 as a

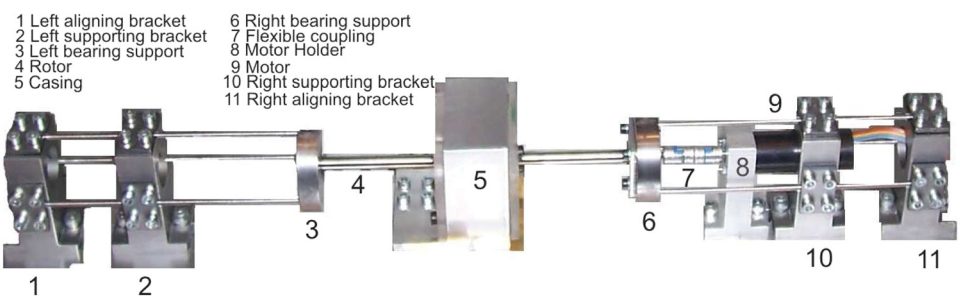

Fig. 12 The complete experimental setup

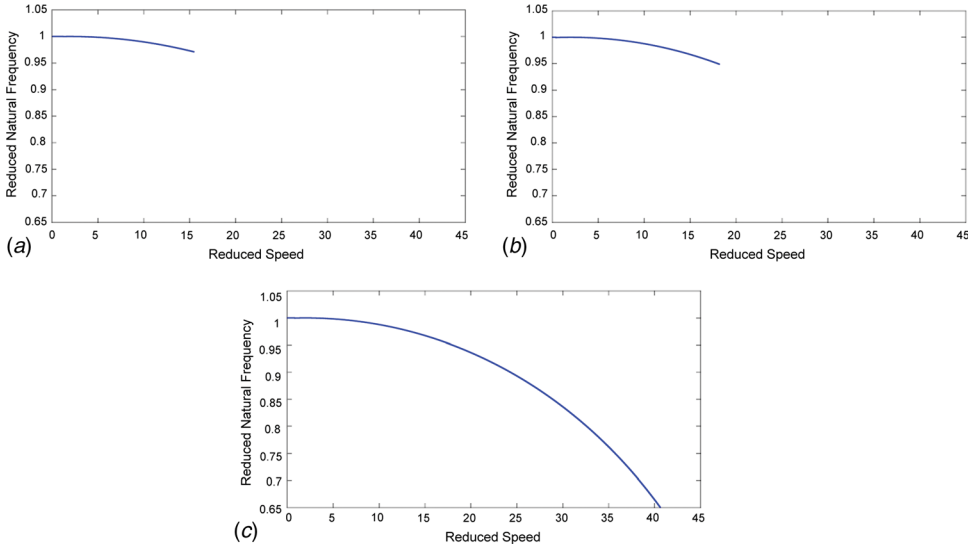

Fig. 13 The reduced natural frequencies for different applications: (*a*) The experimental setup, (*b*) microgenerator, support stiffness: 5×10^4, and (*c*) microgenerator support stiffness: 1×10^4

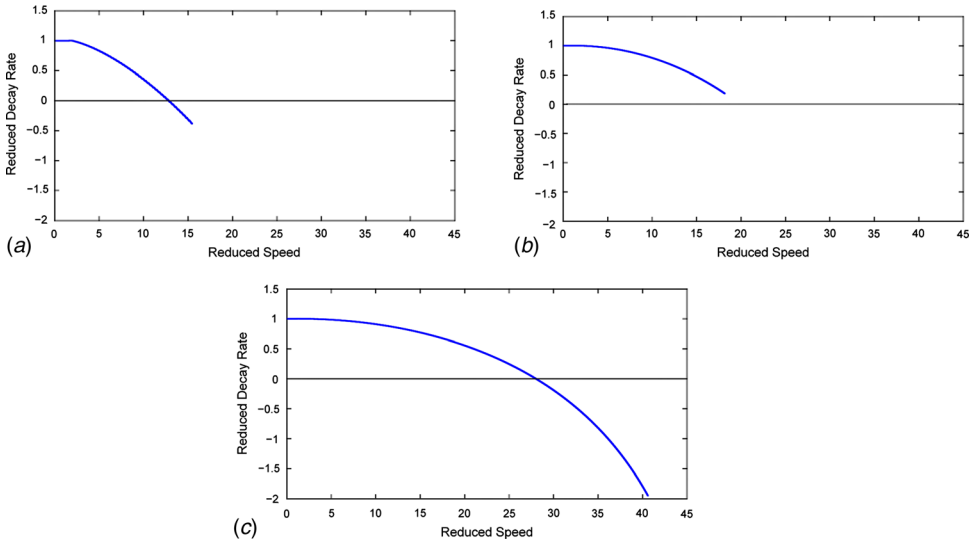

Fig. 14 The reduced decay rate for different applications: (*a*) The experimental setup, (*b*) microgenerator, support stiffness: 5×10^4 and (*c*) microgenerator support stiffness: 1×10^4

function of the reduced rotation speed ($\bar{\Omega}=\Omega/\omega_1$), where ω_1 is the first rigid body mode natural frequency at standstill and σ_1 is the corresponding decay rate.

As can be seen from the Figs. 13 and 14, the support has significant effect on the first natural frequency and the stability of the rotor. Depending on these values, similar reduced velocities and dynamic behavior (reduced natural frequency and decay rate) can be observed between the designed setup and other microrotating machinery with high rotation speeds and low shaft diameters.

6.2 Experiments. At first a modal analysis of the rotor in free-free condition has been performed. This is accomplished by mounting the rotor in flexible cords. The experimental results have been compared with the theoretical results in order to validate the structural model [13]. The results are given in Table 9. Afterward the designed setup is tested for multiphysical effects. As a first step, equivalent support stiffness and damping have

Table 9 First two natural frequencies: theoretical and experimental results at standstill

	Theory	Experiment
First natural frequency	1097.4 Hz	1100.6 Hz
Second natural frequency	1487.0 Hz	1500.5 Hz

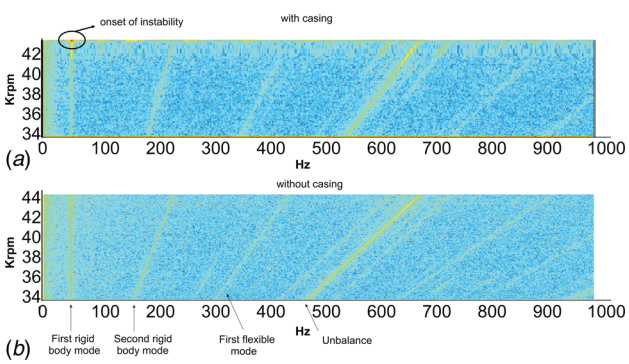

Fig. 15 Spectrum maps-support beam length: 80 mm

Table 10 Experimental and theoretical results for natural frequency and stability

Beam length: 72 mm		Beam length: 80 mm		Beam length: 90 mm	
Rotation speed: 40,000 rpm		Rotation speed: 35,000 rpm		Rotation speed: 25,000 rpm	
Natural frequencies (Hz)		Natural frequencies (Hz)		Natural frequencies (Hz)	
Experiments	Theory	Experiments	Theory	Experiments	Theory
58.1 Hz	61.7 Hz	51.8 Hz	53.4 Hz	44.0 Hz	45.3 Hz
132.8 Hz	141.3 Hz	116.3 Hz	127.9 Hz	100.3 Hz	112.5 Hz
337.8 Hz	328.6 Hz	322.2 Hz	325.8 Hz	315.3 Hz	323.5 Hz
Onset of instability		Onset of instability		Onset of instability	
Experiments	Theory	Experiments	Theory	Experiments	Theory
42,250 rpm	40,200 rpm	41,800 rpm	37,100 rpm	36,250 rpm	30,700 rpm

been calculated from experimental modal analysis of the isolated support [13] and implemented into the structural model. Then, modal analysis and spectrum measurements have been carried out for the assembled system at different support beam lengths. These experiments have been repeated with and without casing in order to observe the multiphysical effects on the dynamic behavior of the rotor. The modal analysis of the setup reveals the natural frequencies. FRF measurements during standstill and operation at different speeds have been performed. The spectrum maps provide information for the determination of the onset instability. Spectrum measurements at different speeds have been done and spectrum maps have been plotted. In order to plot the spectrum maps, rotational speeds are varied in steps of 100 rpm and the velocity of the rotor surface is measured [13]. The experiments have been conducted for support beam lengths of 72 mm, 80 mm, and 90 mm with and without the casing. In this way, the effect of different support properties can be studied. The surrounding air has a negligible effect on the value of the natural frequencies of the system. The onset of instability of the system has been studied by spectrum measurements. The first mode becomes unstable in time and the amplitude in the spectrum at that frequency starts to increase. The surrounding air was observed to cause stability problems. The spectrum maps with and without casing are shown in Fig. 15.

The onset of instability and natural frequencies that were predicted by the theoretical models have been observed in the experiment. The theoretical models are in fair agreement with the experimental results as can be concluded from Table 10. The discrepancy can be a result of accurate measurement problems of stationary damping, adjustment of beam lengths and equivalent support model. However, the difference between the theory and experiment in percentage is similar to the multiphysical rotordynamic studies in literature [26].

7 Conclusions

An experimental setup has been designed in order to validate the numerical model for investigating multiphysical effects on the dynamics of minirotors. The multiphysical effects should be present in the operation range and the designed setup should represent the similar operating conditions (surface velocity and flow type) as the other minirotating machinery. The design criteria have been determined, and the construction of the experimental setup has been executed considering the availability, the simplicity of the components, and the time. Spectrum maps are plotted in order to determine the onset of instability. Unstable operation that was predicted by the theoretical model has been observed during the experiments.

Acknowledgment

The support of MicroNed for this research work is gratefully acknowledged. The authors also would like to thank to Jaap Bulsink for his collaboration throughout the design of the experimental setup.

Nomenclature

C = Damping matrix (N s/m)
C_r = Rotating damping matrix (N s/m)
c_f = Friction coefficient (-)
D_d = Disk diameter (m)
D_s = Shaft diameter (m)
D_{nd} = Near disk diameter (m)
G = Gyroscopic matrix (kg), (kg m ^{2})
H = Gap size (m)
K = Stiffness matrix (N/m), (N/rad)
L = Total length (m)
l = Disk Length (m)
M = Mass matrix (kg), (kg m ^{2})
q = Vector of nodal displacements (m), (rad)
P = eat dissipation due air friction (W)
T_i = Temperature of the ith node (K)
u_{x_i} = Displacement of ith node in x direction (m)
u_{y_i} = Displacement of ith node in y direction (m)
$\hat{\lambda}$ = Complex frequency (-)
ϕ_{x_i} = Rotation of ith node in x direction (rad)
ϕ_{y_i} = Rotation of ith node in y direction (rad)
ρ = Fluid density (kg/m ^{3})
σ = Decay rate (1/s)
$\bar{\sigma}$ = Reduced decay rate (-)
τ = Shear stress on the rotor (Pa)
Ω = Rotation speed (rad/s)
ω = Natural frequency (rad/s)
ω_1 = First rigid body mode natural frequency (rad/s)
$\bar{\omega}$ = Reduced natural frequency (-)

References

[1] Epstein, A., 2004, "Millimeter-Scale, Micro Electro-Mechanical Systems Gas Turbine Engines," ASME J. Eng. Gas Turbines Power, **126**, pp. 205–226.
[2] Frechette, L. G., Jacobson, S., Breuer, K., Ehrich, F., Ghodssi, R., Khanna, R., Wong, C., Zhang, X., Schmidt, M. A., and Epstein, A., 2005, "High-Speed Microfabricated Silicon Turbomachinery and Fluid Film Bearings," J. Microelectromech. Syst., **14**(1), pp. 141–152.
[3] Peirs, J., Reynaerts, D., and Verplaetsen, F., 2004, "A Microturbine for Electric Power Generation," Sens. Actuators, A, **113**, pp. 86–93.
[4] Peirs, J., Reynaerts, D., and Verplaetsen, F., 2003, "Development of an Axial Microturbine for a Portable Gas Turbine Generator," J. Micromech. Microeng., **13**, pp. 190–195.
[5] Isomura, K. and Tanaka, S., 2004, "Development of Micromachine Gas Turbine for Portable Power Generation," JSME Int. J. Ser. B, **43**(3), pp. 459–464.
[6] Sung, T., Han, S., Lee, J., and Jeong, N., 2002, "Designs and Analyses of Flywheel Energy Storage Systems Using High-T_c Superconductor Bearings," Cryogenics, **42**, pp. 357–362.
[7] Lee, E., 2003, "A Micro HTS Renewable Energy/Attitude Control System for Micro/Nano Satellites," IEEE Trans. Appl. Superconduct., **3**(2), pp. 2263–2266.
[8] Zwyssig, C. and Kolar, J., 2006, "Design Considerations and Experimental Results of a 100 w, 500 000 rpm Electrical Generator," J. Micromech. Microeng., **16**, pp. 297–302.

[9] Zwyssig, C., Kolar, J., Thaler, W., and Vohrer, M., 2005, "Design of a 100 w, 500000 rpm Permanent-Magnet Generator for Mesoscale Gas Turbines," *IEEE IAS 2005*, pp. 253–260.
[10] Zwyssig, C., Kolar, J., and Round, S., 2006, "Analytical and Experimental Investigation of a Low Torque, Ultra-High Speed Drive System," *IEEE IAS 2006*, pp. 1507–1513.
[11] Lin, R. M. and Wang, W. J., 2006, "Structural Dynamics of Microsystems-Current State of Research and future Directions," Mech. Syst. Signal Process., **20**, pp. 1015–1043.
[12] Dikmen, E., van der Hoogt, P., de Boer, A., and Aarts, R., 2010, "Influence of Multiphysical Effects on the Dynamics of High Speed Minirotors—Part I: Theory," J. Vibr. Acoust., **132**, p. 031010.
[13] Dikmen, E., van der Hoogt, P., de Boer, A., and Aarts, R., 2010, "Influence of Multiphysical Effects on the Dynamics of High Speed Minirotors—Part II: Results," J. Vibr. Acoust., **132**, p. 031011.
[14] Liu, L., 2005, *Theory for Hydrostatic Gas Journal Bearings for Micro-Electro-Mechanical Systems*, Ph.D. thesis, Massachusetts Institute of Technology, Cambridge, MA.
[15] Teo, C., 2006, *MEMS Turbomachinery Rotordynamics: Modeling, Design and Testing*, Ph.D. thesis, Massachusetts Institute of Technology, Cambridge, MA.
[16] Waumans, T., Vleugels, P., Peirs, J., Al-Bender, F., and Reynaerts, D., 2006, "Rotordynamic Behaviour of a Micro-Turbine Rotor on Air Bearings: Modelling Techniques and Experimental Verification," *Proceedings of ISMA 2006*, Leuven, Belgium, pp. 181–197.
[17] Archer, J., 1965, "Consistent Matrix Formulations for Structural Analysis Using Finite Element Techniques," AIAA J., **3**(10), pp. 1910–1918.
[18] Genta, G., 1985, "Consistent Matrices in Rotor Dynamics," Meccanica, **20**, pp. 235–248.
[19] Genta, G., 2005, *Dynamics of Rotating Systems*, Springer.
[20] Antunes, J., Axisa, F., and Grunenwald, T., 1996, "Dynamics of Rotors Immersed in Eccentric Annular Flow: Part [1]: Theory," J. Fluids Struct., **10**, pp. 897–918.
[21] Saari, J., 1995, *Thermal Modeling of High-Speed Induction Machines*, Electrical Engineering Series, Acta Polytechnica Scandinavica, Helsinki, Finland.
[22] Dikmen, E., van der Hoogt, P., de Boer, A., and Aarts, R., 2009, "Thermal Modeling of a Mini Rotor-Stator System," *ASME 2009 International Mechanical Engineering Congress, Exposition*, ASME.
[23] Vleugels, P., Waumans, T., Peirs, J., Al-Bender, F., and Reynaerts, D., 2006, "High-Speed Bearings for Micro Gas Turbines: Stability Analysis of Foil Bearings," J. Micromech. Microeng., **16**, pp. 282–289.
[24] Lee, Y., Park, D., Kim, C., and Keun, R., 2007, "Rotordynamic Characteristics of a Micro Turbo Generator Supported by Air Foil Bearings," J. Micromech. Microeng., **17**, pp. 297–303.
[25] Tillema, H., 2003, *Noise Reduction of Rotating Machinery by Viscoelastic Bearing Supports*, Ph.D. thesis, University of Twente, The Netherlands.
[26] Grunenwald, T., Axisa, F., Bennett, G., and Antunes, J., 1996, "Dynamics of Rotors Immersed in Eccentric Annular Flow: Part [2]: Experiments," J. Fluids Struct., **10**, pp. 919–944.